



# Titanium dioxide coated zinc oxide nanostrawberry aggregates for dye-sensitized solar cell and self-powered UV-photodetector

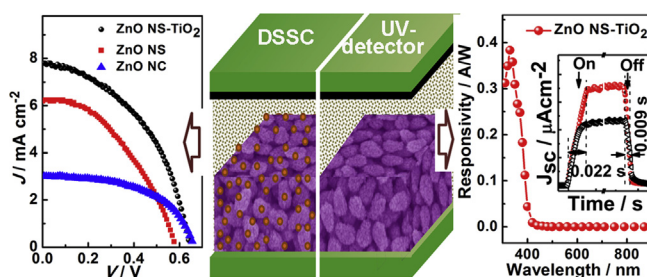
Caitian Gao<sup>\*,1</sup>, Xiaodong Li<sup>1</sup>, Youqing Wang, Lulu Chen, Xiaojun Pan, Zhenxing Zhang, Erqing Xie<sup>\*</sup>

School of Physical Science and Technology, Lanzhou University, Lanzhou, Gansu 730000, PR China

## HIGHLIGHTS

- Preparation of ZnO nanostrawberry aggregates with excellent light scattering.
- ZnO nanostrawberry aggregates film induces large  $J_{sc}$  and PCE in DSSCs.
- Self-powered, ultrafast and visible blind UV detection based on photoelectrochemical cell.

## GRAPHICAL ABSTRACT



## ARTICLE INFO

### Article history:

Received 10 September 2012

Received in revised form

26 March 2013

Accepted 1 April 2013

Available online 8 April 2013

### Keywords:

Zinc oxide nanostrawberry

Dye-sensitized solar cells

Self-powered

UV-photodetector

Light scattering

## ABSTRACT

We report ZnO nanostrawberry aggregates (ZnO NS) structure that serves as photoanode for efficient DSSCs as it offers a large specific surface area, excellent light scattering characteristics, and low degree of charge recombination simultaneously. The short-circuit current density ( $J_{sc}$ ) of the ZnO NS DSSC is more than two times higher than that of commercially-obtained ZnO nanocrystallines (ZnO NC) due to the excellent light scattering of the ZnO NS film, resulting in a 46% improvement in the power conversion efficiency (PCE). The introduction of  $TiO_2$  coating layer on to the ZnO NS (ZnO NS- $TiO_2$ ) results in more than 82% enhancement in the PCE from 1.40% to 2.56%. Moreover, the photoelectrochemical cell (PECC) with unsensitized ZnO NS- $TiO_2$  film as photoanode is applied to detect the UV light without a power source. This self-powered UV-photodetector exhibits a high on/off ratio of 37,900, a fast rise time of 0.022 s and a decay time of 0.009 s for  $J_{sc}$  signal, together with the excellent self-powered, “visible blind” characteristics and photosensitivity linearity in a wide light intensity range.

© 2013 Elsevier B.V. All rights reserved.

## 1. Introduction

Dye-sensitized solar cells (DSSCs) have been regarded as a promising alternative to conventional solid-state semiconductor solar cells due to their facile, low-cost, and environmental-friendly fabrication process [1–3]. Nanostructured metal oxides are one of key factors in determining the power conversion efficiency (PCE) in DSSCs, because nanostructured networks provide a huge surface

area for dye loading and act as a media to transfer photogenerated electrons to the transparent conductive oxide coated electrode. For the DSSCs based on nanocrystalline  $TiO_2$  films, competition between the generation and recombination of photogenerated carriers is a main bottleneck for further increase the PCE [4–6]. Various routes have been developed to solve this problem, such as using one-dimensional nanostructures that are able to provide a direct pathway for the rapid collection of photogenerated electrons and, therefore, reduce the degree of charge recombination [3,7]; using the core-shell structured photoanode to reduce the charge recombination [3,5], and developing many novel three dimensional photoanodes [8–11]. Unfortunately, these routes often lead to

<sup>\*</sup> Corresponding authors. Tel.: +86 931 8912616; fax: +86 931 8913554.

E-mail addresses: [caitiangao10@163.com](mailto:caitiangao10@163.com) (C. Gao), [xieeq@lzu.edu.cn](mailto:xieeq@lzu.edu.cn) (E. Xie).

<sup>1</sup> These authors contributed equally to this work.

insufficient internal surface area and low dye loading for light harvesting.

An efficient way to achieve fast charge transport and slow recombination and simultaneously increase the light harvesting efficiency is to introduce the ZnO aggregates into the photoelectrode film [3,4,12,13]. ZnO is a good alternative of  $\text{TiO}_2$  in DSSCs for its similar relative energy level and band gap but higher electron mobility than  $\text{TiO}_2$  [13,14]. Recently, DSSCs with photoelectrodes made of submicrometer-sized aggregates of ZnO nanocrystallites demonstrated a double PCE as compared to ZnO nanocrystallite DSSCs [3,4]. This improvement accounts for enhanced light scattering and retained high surface area for dye molecule adsorption. However, the efficiencies achieved by ZnO in combination with the ruthenium dye are still low due to dissolve of ZnO by the ruthenium complex. To solve these issues, in this work,  $\text{TiO}_2$  coated ZnO nanostrawberry aggregates (ZnO NS– $\text{TiO}_2$ ) were used as photoanodes for DSSCs. The ZnO NS– $\text{TiO}_2$  DSSC shows great enhancement in PCE than that of the commercially-obtained ZnO nanoparticle (ZnO NC).

Recently, self-powered nanodevices and nanosystems which can function well without an external power source have attracted more and more attentions [15–18]. Photovoltaic devices convert light energy into electricity with the use of a photon–electron excitation process in semiconductor materials, therefore, photovoltaics are natural photodetectors and can operate without external power sources, in other words, they are self-powered photodetectors [18–20]. Among various photovoltaics, the photoelectrochemical cell (PECC) with a similar configuration to DSSCs but without dye adsorption is more promising due to it has the same key advantages as those of DSSCs [18]: low-cost, simple manufacturing process, composed of abundant and non-toxic raw materials, and more economical due to dispense with dyes. In our previous work, we demonstrated the application of a nanocrystalline  $\text{TiO}_2$  film based PECC as a self-powered UV-photodetector to detect the UV light without a power source [18]. This PECC is of a standard design of DSSCs, except that no dye molecules are adsorbed. In principle, the energetics of operation of the UV-photodetector is similar to that of a DSSC [18]. Therefore, ZnO NS– $\text{TiO}_2$  should also be an efficient photoanode for such PECC.

## 2. Experimental

### 2.1. Preparation of ZnO nanostrawberry aggregates

Preparation of ZnO NS was similar to a two-stage reaction process reported previously [21,22]. To prepare ZnO NS and ZnO nanosphere aggregates (ZnO NP), the submergence ratio (the depth of the reaction solution in oil level to the solution height) was controlled to be 50% and 100%, respectively, as shown in Fig. 1. Firstly, ZnO seeds were formed by hydrolysis of 1.31 g of zinc acetate dehydrate ( $\text{Zn}(\text{OAc})_2$ ) in 60 mL of diethylene glycol (DEG). The reaction solution was heated to 180 °C (50% submergence ratio) and 165 °C (100% submergence ratio) under vigorous magnetic stirring, precipitation of ZnO occurred after reaching the responding working temperature. Then the product was cooled down to room temperature naturally and the supernatant was saved after centrifugation at 3000 rpm for 30 min. Thirdly, a secondary reaction began in the same way as the primary reaction: 1.31 g  $\text{Zn}(\text{OAc})_2$  was added to 60 ml DEG and the reaction solutions were heated under vigorous magnetic stirring. Prior to reach the working temperature, typically 155 °C, the primary reaction supernatants were added to the two solutions. At last the two solutions were heated to 180 °C and kept at this temperature for 2 h.

### 2.2. Fabrication of ZnO NS– $\text{TiO}_2$ core–shell photoanodes

To obtain ZnO NS– $\text{TiO}_2$  core–shell photoanodes, the ZnO NS (0.06 g) were ultrasonically dispersed in a mixture (0.25 g) containing acetic acid, deionized water and ethanol (volume ratio of 1: 33: 66) for durations of 10 min. Then the pastes were coated on F-doped tin oxide (FTO) glass substrates (with >80% transmittance, 7  $\Omega$  per square for DSSCs and >90% transmittance, 14  $\Omega$  per square for self-powered UV-photodetectors, 2.2 mm in thickness, Nippon, Japan) by drop-drying method. The thickness of the films was fixed at  $\sim 10 \mu\text{m}$ , which was measured from the cross sectional SEM image of a ZnO NS– $\text{TiO}_2$  film (see Fig. S1(a)). The films were sintered at 450 °C for 60 min. Finally,  $\text{TiO}_2$  was coated on ZnO by a drop-drying method followed by annealing at 450 °C for 1 h. The

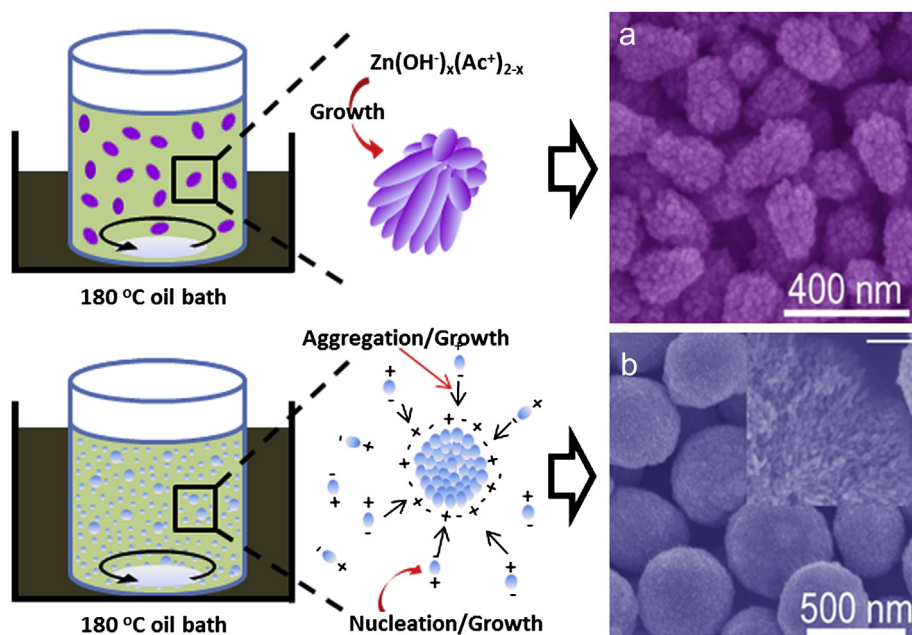
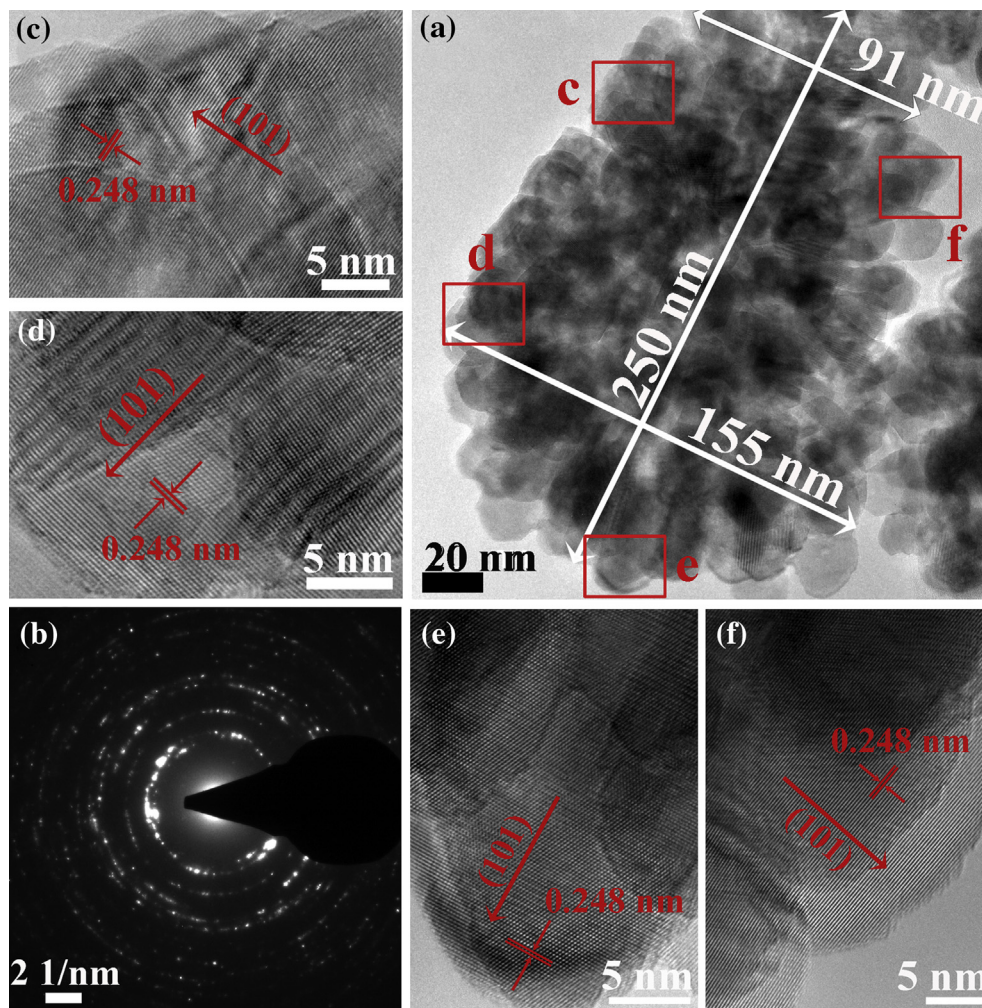


Fig. 1. Schematic diagram of the formation mechanism of strawberry-like and sphere-like ZnO aggregates, the corresponding SEM images are shown in (a) and (b).



**Fig. 2.** (a) and (b) are TEM image and SAED pattern of a single strawberry-like ZnO aggregate, respectively. (c)–(f) are high-resolution TEM images corresponding to the areas marked as c, d, e and f in Fig. 2(a).

coating solution was 20 mM tetrabutyl titanate and 10 mM monoethanolamine in ethanol.

### 2.3. Assembling of DSSCs and self-powered UV-photodetectors

The details of the assembling process of DSSCs have been described in our previous work [5,18]. In brief, the sintered electrodes were sensitized by immersing them into a 0.3 mM solution of N-719 dye in a mixture of tert-butyl alcohol and acetonitrile (volume ratio of 1: 1) for 3 h in the dark. The counter electrodes were prepared by spin-coating a 60 mM isopropanol solution of  $\text{H}_2\text{PtCl}_6 \cdot 6\text{H}_2\text{O}$  on FTO glass (>80% transmittance,  $7 \Omega$  per square, 2.2 mm in thickness, Nippon, Japan) followed by sintering at  $400^\circ\text{C}$  for 20 min. The interelectrode space was filled with a liquid electrolyte consisting of 0.1 M LiI, 0.6 M 1, 2-dimethyl-3-propylimidazolium iodide, 0.05 M  $\text{I}_2$  and 0.5 M 4-tert-butylpyridine in acetonitrile. The effective area of DSSCs was fixed at  $0.21 \text{ cm}^2$ . The unsensitized films were used as photoanodes for self-powered UV-photodetectors, and the assembling process is similar to that of DSSCs.

### 2.4. Characterizations

The morphology and structure of the samples were characterized by field emission scanning electron microscopy (FE-SEM, Hitachi S-4800) and transmission electron microscopy (TEM, FEI

Tecnai F30). X-Ray diffraction (XRD, Philips, X'pert pro, Cu K $\alpha$ , 0.154056 nm) was employed to characterize the structural properties of the samples. Raman scattering spectra were carried out on a Jobin-Yvon LabRam HR80 spectrometer (with a 532 nm line of Torus 50 mW diode-pumped solid-state laser) under the back-scattering geometry at room temperature. The optical properties were studied by a UV–VIS spectrophotometer (TU-1901). Photovoltaic performance and electrochemical impedance spectroscopy (EIS) of the devices were obtained on an Electrochemical Workstation (RST5200, Zhengzhou Shiruishi Instrument Technology Co., Ltd, China). EIS measurements were carried out in the frequency range of 0.01 Hz–100 kHz at open-circuit voltage with a potential pulse of 10 mV in amplitude. A UV detector (ST-513, UVAB, SENTRY OPTRONICS CORP., Taiwan) was used to quantify UV irradiance. A 500 W Xenon lamp equipped with a monochromator and an ultraviolet band pass filter (365 nm) was used as light source.

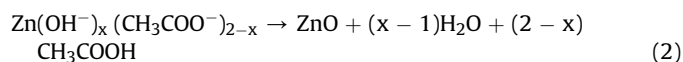
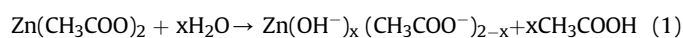
## 3. Results and discussion

### 3.1. Formation and characterization of the ZnO nanostrawberry aggregates

Fig. 1 shows the SEM images and schematic diagram of the formation mechanism of ZnO NS and ZnO NP. As shown in Fig. 1(b), ZnO NP were formed from numerous nanoparticles  $\sim 19 \text{ nm}$  in



diameter, and the primary nanoparticles appear to be oriented radially from the center of the aggregate (inset in Fig. 1(b)). However, the ZnO NS were formed from numerous primary nanoparticles  $\sim 22$  nm in diameter, as seen on the surface morphology (Fig. 1(a)). To illuminate the special substructure of ZnO NS, TEM image of a single ZnO NS is shown in Fig. 2(a). It can be seen that the primary particles are rod-like and are radially agglomerated with an average big side of  $\sim 155$  nm, an average small side of  $\sim 91$  nm, and an average length of  $\sim 250$  nm. The high-resolution TEM images corresponding to the areas marked as c, d, e and f in Fig. 2(a) are shown in Fig. 2(c)–(f), respectively. It is necessary to note that all the growth directions of the radially arranged rod-like ZnO are along [101], which agrees with the dominant [101] growth direction in XRD spectrum of the hexagonal wurtzite structure ZnO aggregates (Fig. 3(a)). SAED characterization of a single ZnO aggregate indicates that they are polycrystallines. Based on the above results, we propose a mechanism to explain the formation of the ZnO NS. In our experiments, preparation process of such ZnO NS is similar to that of ZnO NP [21,22], except that the submergence ratio is controlled at 50%. Therefore, the temperature fluctuation resulted from the vigorous magnetic stirring and half submergence of the reaction solution play key roles. When the mixed reaction solution is heated to  $110^\circ\text{C}$ , reactions are ascribed as the following equations [23]:



Eq. (1) is the hydrolysis reaction of  $\text{Zn}(\text{OAc})_2$  to form metal complexes. Eq. (2) is dehydration and removal of acetic acid to form pure ZnO. For ZnO NP, when increasing the temperature to  $\sim 160^\circ\text{C}$ , a number of nuclei were generated due to the supersaturation upon chemical reaction. These nuclei grow and develop

into ovoid-like nanoparticles (Inset in Fig. 1(b)). The nanoparticles and the seeds added at  $155^\circ\text{C}$  are in a non-equilibrium state because of the weak electrical double layers that lead to inadequate repulsion between these nanoparticles, resulting in aggregation [24]. Because the spherical aggregates have the minimum surface energy and electrical potential, ovoid-like ZnO nanoparticles aggregate into sphere-like ZnO aggregates by dipole interactions to minimize interfacial energy. However, for the ZnO NS, the nucleation process is retarded and the grow process is dominated due to temperature fluctuation. In this case, when the temperature is increased from  $155^\circ\text{C}$  to  $180^\circ\text{C}$  and aging, the Zn complexes would dehydrate and remove acetic acid to form pure ZnO as Eq. (2) with the seeds as nuclei centers. At first, the growth is mainly along the [101] face of the ZnO seeds and the growth along other faces is very slow, which results in the formation of big side of the “strawberry” consisting of rod-like ZnO primary particles. During the growth, the nuclei generate on the other faces of the seeds and [101] face is gradually become dominate along these directions, resulting in the formation of the small side of “strawberry”. At last, ZnO NS with all the growth directions along [101] is formed.

### 3.2. Morphology and structure of ZnO NS–TiO<sub>2</sub>

The coating of TiO<sub>2</sub> layer on the surface of ZnO is presumably too thin to affect any detectable change in the morphology by means of SEM, as illustrated in Fig. 1(b) and Fig. S1(a), Supporting Information. XRD and Raman spectroscopy were carried out on ZnO and ZnO–TiO<sub>2</sub> film at room temperature to investigate their structure information. Fig. 3(a) compares the XRD spectra of ZnO with that of ZnO–TiO<sub>2</sub>. All diffraction peaks of ZnO can be well indexed to a wurtzite structure of ZnO (JCPDS no.36-1451). In the case of the ZnO NS–TiO<sub>2</sub> film, no additional peak characteristic of TiO<sub>2</sub> was observed. Fig. 3(b) shows Raman scattering spectra of ZnO and ZnO–TiO<sub>2</sub> films. ZnO NS shows three distinct peaks at 327, 433 and  $580\text{ cm}^{-1}$ , which should be assigned accordingly to  $E_2(\text{high})$ – $E_2(\text{low})$ ,  $E_2(\text{high})$  and superimposition of  $A_1(\text{LO})$  and  $E_1(\text{LO})$  mode of ZnO [25], respectively. After TiO<sub>2</sub> coating, only one peak at  $433\text{ cm}^{-1}$  overlapped with a broad amorphous band is identifiable, the other two peaks have been diminished. These results verify the presence of amorphous TiO<sub>2</sub> coating on the surface of ZnO NS. Further insight into the structural information was obtained by HRTEM taken from the ZnO/TiO<sub>2</sub> interface, as shown in inset of Fig. 4. The HRTEM image reveals the uniform shell formation around ZnO with a TiO<sub>2</sub> layer thickness of  $\sim 3$  nm. The TiO<sub>2</sub> shell is amorphous, agreeing with the results concluded from Raman scattering spectra.

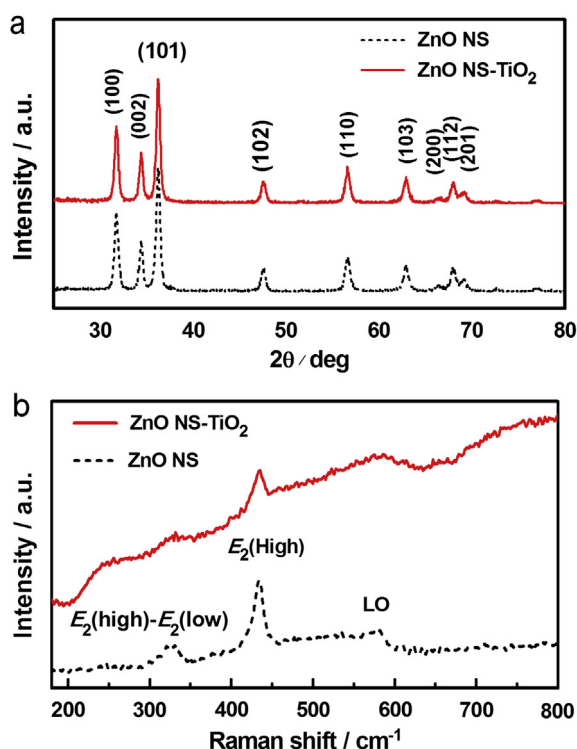


Fig. 3. XRD (a) and Raman scattering (b) spectra of ZnO NS and ZnO NS–TiO<sub>2</sub>.

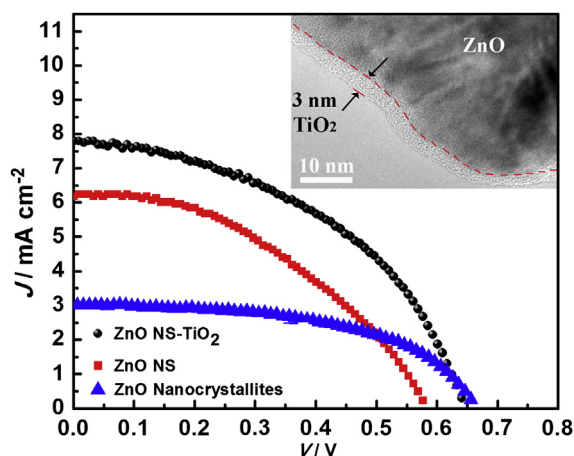


Fig. 4.  $J$ – $V$  curves of DSSCs with the photoelectrode films of ZnO NS–TiO<sub>2</sub>, ZnO NS and ZnO NC. Inset is HRTEM image of ZnO NS–TiO<sub>2</sub> taken from ZnO/TiO<sub>2</sub> interface.

### 3.3. The performance of DSSCs

The photovoltaic performances of ZnO NS–TiO<sub>2</sub> DSSCs were tested under an illumination condition of one sun (AM 1.5 G, 100 mW cm<sup>-2</sup>) and compared with those of pure ZnO NS and commercially-obtained ZnO nanoparticles (ZnO NC). The characteristic *J*–*V* curves of these DSSCs are presented in Fig. 4, and the corresponding photovoltaic parameters are summarized in Table 1. It can be seen that the average open-circuit photovoltage (*V*<sub>oc</sub>) and short-circuit photocurrent density (*J*<sub>sc</sub>) of ZnO NS–TiO<sub>2</sub> DSSCs (*V*<sub>oc</sub> = 0.664 V, *J*<sub>sc</sub> = 7.66 mA cm<sup>-2</sup>) are considerably higher than those of the ZnO NS DSSCs (*V*<sub>oc</sub> = 0.601 V, *J*<sub>sc</sub> = 6.13 mA cm<sup>-2</sup>). These results are expected because (1) TiO<sub>2</sub> coating on ZnO prevents the dissolving of ZnO by the ruthenium complex to form random aggregates [26], which leads to an increased charge-injection efficiency and a higher *J*<sub>sc</sub>; and (2) a built-in potential resulting from the electron concentration gradient between the ZnO core and TiO<sub>2</sub> shell due to their size difference, which can confine the electrons in the ZnO core and eventually resulting in a suppressed recombination and a higher *V*<sub>oc</sub> [13]. Of course, the presence of TiO<sub>2</sub> does not favor the electron transfer from TiO<sub>2</sub> shell to ZnO core due to the higher conduction band edge of TiO<sub>2</sub> than ZnO. However, the thickness of the TiO<sub>2</sub> shell is only 3 nm (see HRTEM image in inset of Fig. 4), which allows tunneling of the forward current while suppressing recombination. Moreover, the presence of TiO<sub>2</sub> results in a better stability of the cells with time, as shown in Fig. S2.

The distinct photovoltaic behavior of the ZnO–NS DSSC is that its *J*<sub>sc</sub> is more than twice as large as that of ZnO NC DSSC. One reason for the increase of *J*<sub>sc</sub> is the enhanced absorption behavior associated with the presence of large nanostrawberry ZnO aggregates, resulting in higher photon absorption by way of light scattering. Fig. 5 compares the variation in the absorption behavior of ZnO NS film with that of ZnO NC film. According to the scattering theory, effective Mie scattering happens to the particles with size in the range of light wavelengths. Therefore, the enhanced absorption shown in visible range for ZnO NS film is due to light scattering of the ZnO aggregates. The light scattering of the ZnO aggregates would increase the light path length in the ZnO NS film, and consequently enhance the light harvesting efficiency, resulting in an increase of *J*<sub>sc</sub>, which is in accordance to previous reports [4,12,27]. Another reason is due to the more efficient electrolyte transport through the ZnO NS film than that of the ZnO NC film. It is demonstrated that the large interspaces among the large aggregates can act as “relay stations” for electrolyte diffusion, which can help ions transport through the film more efficiently [2,28], resulting in an increase of *J*<sub>sc</sub>.

To reveal the differences between the interfacial characteristics of these photoelectrodes, we measured EIS spectra of DSSCs using ZnO NS–TiO<sub>2</sub>, ZnO NS and ZnO NC, as shown in Fig. 6. In all the EIS spectra, three well-defined semicircles, denote the redox reaction of I<sup>-</sup>/I<sub>3</sub><sup>-</sup> at the Pt/electrolyte interface, the electron transfer at the oxide/dye/electrolyte interface and the diffusion impedance of the

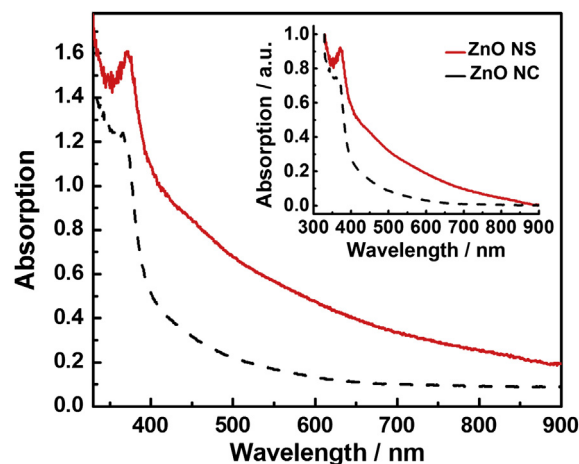


Fig. 5. The absorption behavior of ZnO films on FTO, inset shows the normalized absorption curves with an arbitrary unit.

electrolyte according to recent analysis on the EIS spectra of DSSCs [29], were observed in the region of 100,000–1000 Hz, 1000–1 Hz and 1–0.01 Hz, respectively. The lifetime of the electrons in the oxide film ( $\tau_r$ ) can be estimated from the characteristic frequencies of the impedance semicircle at middle frequencies, according to the relation  $\tau_r = 1/2\pi f_{\max}$ , where  $f_{\max}$  is the maximum frequency of the mid-frequency peak. As shown in the inset of Fig. 6, the  $f_{\max}$  value for ZnO NS–TiO<sub>2</sub> is 16.2 Hz, much smaller than the values for ZnO–NS (28.1 Hz) and ZnO–NC (42.5 Hz), indicating a longer electron lifetime in ZnO NS–TiO<sub>2</sub> film than that in ZnO NS and ZnO NC film. There is no doubt that the longer electron lifetime enables ZnO NS based films to achieve higher PCE.

### 3.4. The performance of self-powered UV-photodetectors

Fig. 7(a) shows a diagram of the UV-photodetector. It is of a standard design of DSSCs, except that no dye molecules are adsorbed. Fig. 7(b) shows energetics of operation of the UV-photodetector with ZnO NS–TiO<sub>2</sub> film as photoanode, which is similar to that of a nanocrystalline TiO<sub>2</sub> film based PECC [18]: Current is generated when a UV photon is absorbed by wide band gap semiconductors, such as ZnO in this work, rather than by the dye molecules adsorbed on the surface of the semiconductors; the photons with energy larger than its band gap promote electrons

Table 1

Comparison of short-circuit photocurrent density (*J*<sub>sc</sub>), open-circuit photovoltage (*V*<sub>oc</sub>), fill factor (FF), power conversion efficiency (PCE) and the maximum frequency of the mid-frequency peak ( $f_{\max}$ ) of EIS for the DSSCs with ZnO NS–TiO<sub>2</sub>, ZnO NS, and ZnO NC films as photoelectrodes. Each value of *J*<sub>sc</sub>, *V*<sub>oc</sub>, FF and PCE for ZnO NS–TiO<sub>2</sub> and ZnO NS was an average of three measurements.

Films	<i>J</i> <sub>sc</sub> [mA cm <sup>-2</sup> ]	<i>V</i> <sub>oc</sub> [V]	FF	PCE [%]	$f_{\max}$ [Hz]
ZnO NS–TiO <sub>2</sub>	7.66 ± 0.45	0.664 ± 0.021	0.504 ± 0.054	2.56 ± 0.23	16.2
ZnO NS	6.13 ± 0.16	0.601 ± 0.018	0.378 ± 0.038	1.40 ± 0.13	28.1
ZnO NC	3.01	0.660	0.531	1.05	42.5

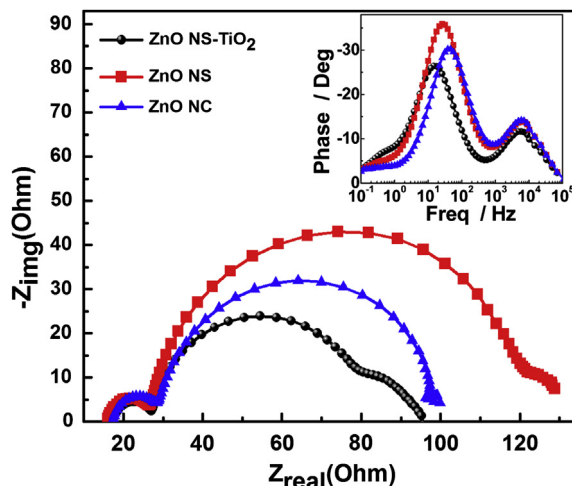


Fig. 6. EIS of DSSCs with the photoelectrode films of ZnO NS–TiO<sub>2</sub>, ZnO NS and ZnO NC. Inset displays the Bode phase plot of the three films.

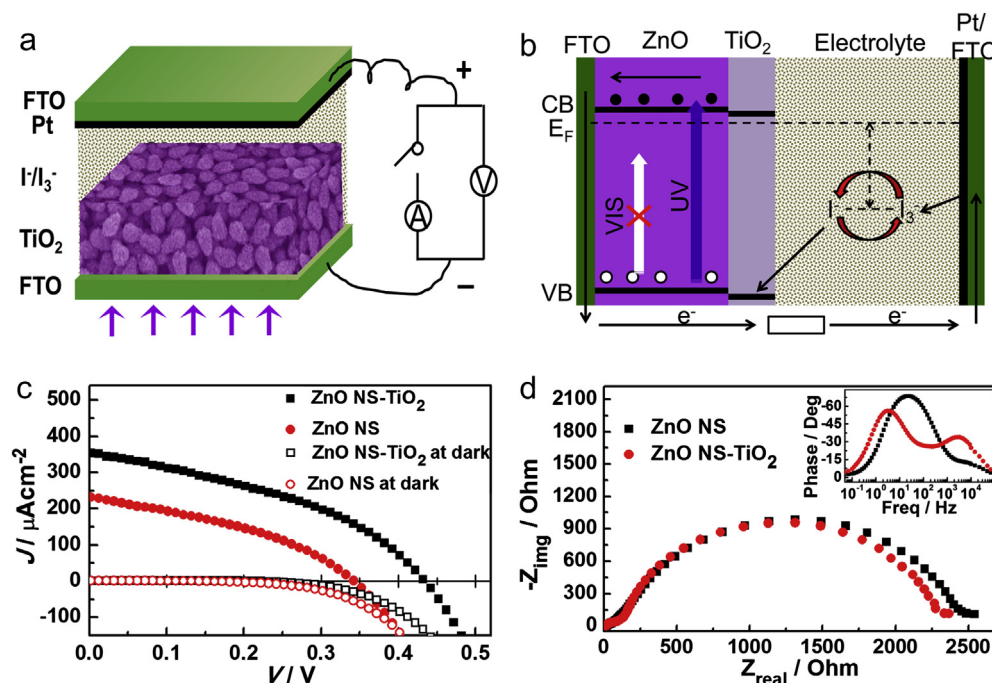
from the valence band (VB) to conduction band (CB), leaving behind a hole; the hole migrates to the  $\text{TiO}_2$ /electrolyte interface, where it oxidizes an electron donor in electrolyte; the resulting oxidized species are then reduced by electrons from external circuit at the counter electrode, completing the circuit. Here, the presence of  $\text{TiO}_2$  does not favor the hole transport from  $\text{TiO}_2$  to electrolyte because the top of valence band of  $\text{TiO}_2$  is lower than ZnO. However, this influence is weak because the thickness of the  $\text{TiO}_2$  shell is only 3 nm. While it has no influence on electrons transport although the conduction band edge of  $\text{TiO}_2$  is higher than ZnO. This is because in such a device with unsensitized photoanode, the light is absorbed by ZnO and the generated electrons transferred in ZnO core, no electron needs to transfer from  $\text{TiO}_2$  shell to ZnO core. On the other hand, as mentioned above, the presence of  $\text{TiO}_2$  can confine the electrons in the ZnO core and eventually resulting in a suppressed recombination. In summary, the presence of  $\text{TiO}_2$  on ZnO will improve the performance of UV-photodetectors.

$J$ – $V$  curves shown in Fig. 7(c) were measured under  $20 \text{ mA cm}^{-2}$  UV light ( $\lambda = 365 \text{ nm}$ ) for PECCs with ZnO NS– $\text{TiO}_2$  and ZnO NS films as photoanodes. As expected, ZnO NS– $\text{TiO}_2$  gives a higher  $J_{sc}$  value of  $357 \mu\text{A cm}^{-2}$  than  $234 \mu\text{A cm}^{-2}$  for ZnO NS. This value is also higher than that of the nanocrystalline  $\text{TiO}_2$  film based PECC ( $301 \mu\text{A cm}^{-2}$  [18]), indicating a high photosensitivity. To investigate the source of the increase of  $J_{sc}$  after  $\text{TiO}_2$  coating, we measured EIS of the PECCs using ZnO NS– $\text{TiO}_2$  and ZnO–NS, as shown in Fig. 7(d). Both of the Nyquist plots show two well-defined semicircles, denotes the redox reaction of  $\text{I}^-/\text{I}_3^-$  at the Pt/electrolyte interface and electron transfer at the oxide/dye/electrolyte interface. Similar to the EIS of DSSCs, the lifetime of the electrons in the oxide film ( $\tau_r$ ) can be estimated from the characteristic frequencies of the impedance semicircle at middle frequencies, according to the relation  $\tau_r = 1/2\pi f_{\text{max}}$ . As shown in the inset of Fig. 7(d), the  $f_{\text{max}}$  value for the ZnO NS– $\text{TiO}_2$  is 3.18 Hz, much smaller than the values for ZnO–NS (23.68 Hz), indicating a longer electron lifetime in ZnO

NS– $\text{TiO}_2$  film than in ZnO NS film. Therefore, the longer electron lifetime enables ZnO NS– $\text{TiO}_2$  film to achieve higher  $J_{sc}$  signal in such a self-powered UV-photodetector based on the photovoltaic effect of PECCs.

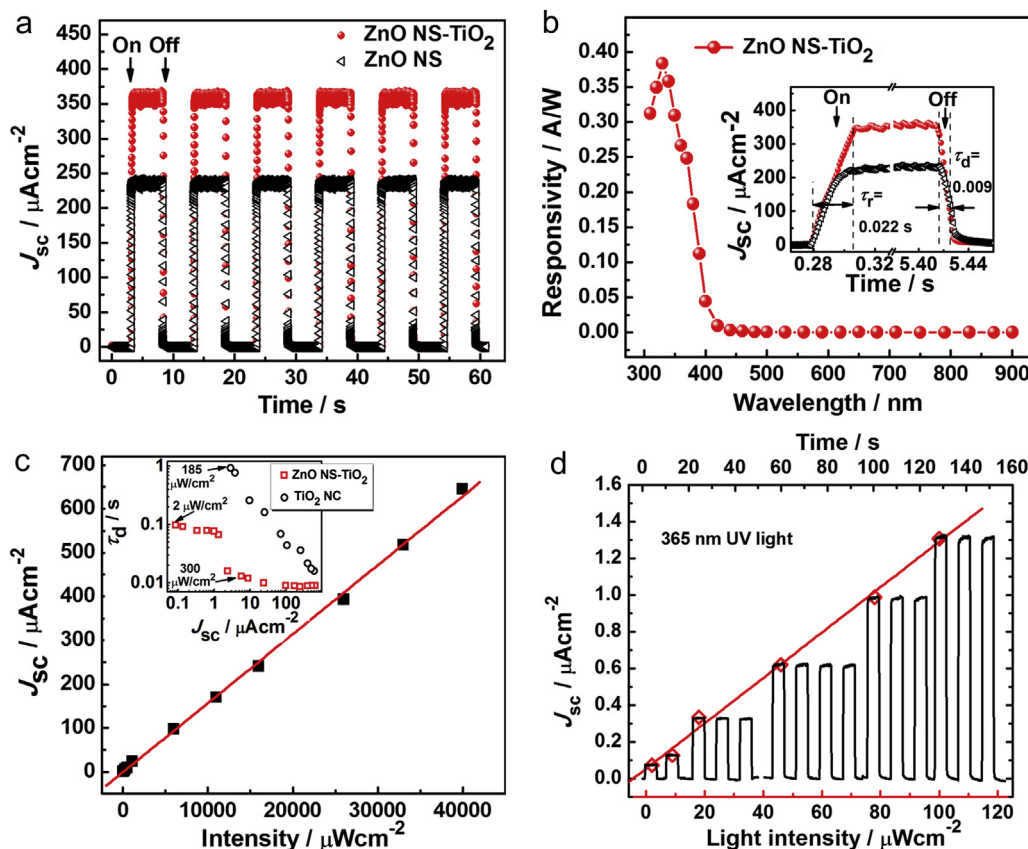
The photoresponse switching behaviors of the PECCs are shown in Fig. 8(a). It can be observed that the  $J_{sc}$  can be reproducibly switched from the “ON” state to the “OFF” state by periodically turning the UV light on and off with a power density of  $20 \text{ mW cm}^{-2}$  and the wavelength of 365 nm. The on/off ratios of the  $J_{sc}$  signal of the two devices, defined as  $I_{\text{light}}/I_{\text{dark}}$ , are found to be about 37,900 for ZnO NS– $\text{TiO}_2$  and 11,700 for ZnO NS. From the enlarged rising and recovering edge of the current responses which is shown in the inset of Fig. 8(b), the rise time ( $\tau_r$ ) and the decay time ( $\tau_d$ , defined as time to recovery to  $1/e$  (37%) of the maximum photocurrent) of the device are 0.022 and 0.009 s for  $J_{sc}$ , respectively. Such fast photoresponse of  $J_{sc}$  is much superior to the photoconductivity-based UV-photodetectors made by 1D  $\text{TiO}_2$  and ZnO nanostructures [30–33]; and also faster than the values of PECCs based on nanocrystalline  $\text{TiO}_2$  film ( $\tau_r$  0.08 s and  $\tau_d$  0.03 s) [18] and  $\text{TiO}_2/\text{SnO}_2$  branched heterojunction electrode ( $\tau_r$  0.03 s and  $\tau_d$  0.01 s) [34].

Fig. 8(b) shows the spectral response of ZnO NS– $\text{TiO}_2$  PECC. The responsivity measures the electrical output per optical input of a photodetector, usually expressed in units of amperes per watt of incident radiant power (A/W). The peak responsivity is located at 330 nm with a high value of  $\sim 0.38 \text{ A/W}$ , which is approximately equal to that of a nanocrystalline  $\text{TiO}_2$  film based PECC [18]. For comparison, the responsivity of most commercial UV-photodetectors is in the range of 0.1–0.2 A/W [35]. This spectral response exhibits that the device has excellent UV photoresponse, allowing dispense with the high-precision measurement systems for detecting the signal. The responsivity during the visible region drops 2,665 times for  $J_{sc}$  as compared with the peak, indicating that the device can be used as visible blind UV-photodetector. In our



**Fig. 7.** (a) Schematic of self-powered UV-photodetector based on photoelectrochemical cell with ZnO NS– $\text{TiO}_2$  film as photoanode. (b) Energetics of operation of the UV-photodetector. The open-circuit voltage ( $V_{oc}$ ) corresponds to the difference between the quasi-Fermi level of ZnO under illumination and the electrochemical potential of electrolyte.  $J$ – $V$  curves (c) and EIS (d) of the self-powered UV-photodetectors with the photoelectrode films of ZnO NS– $\text{TiO}_2$  and ZnO NS. The inset displays the Bode phase plot of the two films.





**Fig. 8.** (a) Time responses of  $J_{sc}$  upon 20 mW cm<sup>-2</sup> UV light illumination ( $\lambda = 365$  nm) measured for light on and -off states. The rising and recovering edge of the current response is magnified in the inset of (b). (b) Spectral responses of the self-powered UV-photodetector with the photoelectrode films of ZnO NS-TiO<sub>2</sub>. The measurement was carried out under the light intensity of 50 μW cm<sup>-2</sup>. (c)  $J_{sc}$  as a function of the incident UV ( $\lambda = 365$  nm) intensity. Inset compares the decay time of ZnO NS-TiO<sub>2</sub> with that of TiO<sub>2</sub> NC PECC as a function of  $J_{sc}$ . (d) Shows photosensitivity linearity and photoresponse switching behavior under low light intensity from 2 μW m<sup>-2</sup> to 100 μW cm<sup>-2</sup>.

previous work [18,34,36], we observed responses in the visible region for PECCs based on nanocrystalline TiO<sub>2</sub> film and TiO<sub>2</sub>/SnO<sub>2</sub> branched heterojunction electrode, which originated from the trap-to-trap electron transport due to the existence of trap states in TiO<sub>2</sub> and SnO<sub>2</sub>. However, no response is found in ZnO NS based PECC. This advantage makes ZnO NS based PECC to be more suitable in visible-blind UV-photodetectors.

Another key property for applications of the photodetectors is the dependence of  $J_{sc}$  on the intensity of the incident UV light. As shown in Fig. 8(c) and (d), the  $J_{sc}$  increases linearly with increasing the UV light intensity in a wide variation range from 2 μW cm<sup>-2</sup> to 40 mW cm<sup>-2</sup>. Moreover, this UV-photodetector shows a good photosensitivity and photoresponse switching behavior even under low light intensity from 2 μW cm<sup>-2</sup> to 100 μW m<sup>-2</sup>, Fig. 8(d). The on/off ratios of the  $J_{sc}$  signal under an ultralow light intensity of 2 μW cm<sup>-2</sup> is as high as 68, indicating an excellent UV response behavior under low light intensity. It is reported that DSSCs usually show a light intensity dependent decay time under a short-circuit condition owing to the trapping/detrapping events of the electrons [5,6]. Therefore, we measured light intensity dependent decay time of the ZnO NS-TiO<sub>2</sub> PECC at a short-circuit condition and compared to that of TiO<sub>2</sub> NC PECC, as shown in inset of Fig. 8(c). It can be observed that the  $\tau_d$  keeps constant at less than 0.01 s when the light intensity is larger than 300 μW cm<sup>-2</sup>, followed by gradually increasing to <0.1 s under the ultralow light intensity of 2 μW cm<sup>-2</sup>. While the  $\tau_d$  for TiO<sub>2</sub> NC increases linearly to ~0.9 s under a light intensity of 185 μW cm<sup>-2</sup>, indicating more excellent UV time response property of ZnO NS-TiO<sub>2</sub> PECC than that of TiO<sub>2</sub>

NC, especially under low light intensity. Moreover, such values under low light intensity are still superior to most of the photoconductivity-based UV-photodetectors made by 1D TiO<sub>2</sub> and ZnO nanostructures [30–33].

#### 4. Conclusion

In conclusion, the ZnO nanostrawberry aggregates were prepared by a two-stage reaction process with submergence ratio is controlled to 50%. The temperature fluctuation resulted from the vigorous magnetic stirring and half submergence of the reaction solution play key roles in the formation of the ZnO NS. The  $J_{sc}$  of the ZnO NS DSSC is more than twice as high as that of ZnO NC DSSC. Further enhancement in the PCE was achieved by introducing TiO<sub>2</sub> coating layer on ZnO NS, with more than 82% enhancement from 1.40% to 2.56%. Configured as self-powered UV-photodetectors, the PECC with unsensitized ZnO NS-TiO<sub>2</sub> film as photoanode exhibits a high on/off ratio of 37,900, a fast rise time of 0.022 s and a decay time of 0.009 s for  $J_{sc}$  signal. The fast time response, high photosensitivity, and good photosensitivity linearity combined with low-cost, environment-friendly, as well as the facile manufacturing process, make this new type of UV-photodetector suitable for practical applications.

#### Acknowledgement

This work was financially supported by the National Natural Science Foundation of China (No. 61176058), partially by Natural

Science Foundation of Gansu Province (1107RJYA280) and Fundamental Research Funds for the Central Universities (No. lzujbky-2012-34).

## Appendix A. Supplementary data

Supplementary data related to this article can be found online at <http://dx.doi.org/10.1016/j.jpowsour.2013.04.003>.

## References

- [1] B. O'Regan, M. Grätzel, *Nature* 353 (1991) 737.
- [2] X. Li, Y. Zhang, Z. Zhang, J. Zhou, J. Song, B. Lu, E. Xie, W. Lan, J. Power Sources 196 (2011) 1639.
- [3] Q. Zhang, G. Cao, *Nano Today* 6 (2011) 91–109.
- [4] Q. Zhang, T. Chou, B. Russo, S. Jenekhe, G. Cao, *Angew. Chem. Int. Ed.* 47 (2008) 2402–2406.
- [5] C. Gao, X. Li, B. Lu, L. Chen, Y. Wang, F. Teng, J. Wang, Z. Zhang, X. Pan, E. Xie, *Nanoscale* 4 (2012) 3475–3481.
- [6] J.H. Noh, H.S. Han, S. Lee, J.Y. Kim, K.S. Hong, G.-S. Han, H. Shin, H.S. Jung, *Adv. Energy Mater.* 1 (2011) 829–835.
- [7] L. Li, T. Zhai, Y. Bando, D. Golberg, *Nano Energy* 1 (2012) 91–106.
- [8] C.S. Rustomji, C.J. Frandsen, S. Jin, M.J. Tauber, *J. Phys. Chem. B* 114 (2010) 14537–14543.
- [9] X. Fan, F. Wang, Z. Chu, L. Chen, C. Zhang, D. Zou, *Appl. Phys. Lett.* 90 (2007) 073501–073503.
- [10] Y. Xiao, J. Wu, G. Yue, J. Lin, M. Huang, L. Fan, Z. Lan, J. Power Sources 208 (2012) 197–202.
- [11] W. Guo, C. Xu, G. Zhu, C. Pan, C. Lin, Z.L. Wang, *Nano Energy* 1 (2012) 176–182.
- [12] T.P. Chou, Q. Zhang, G.E. Fryxell, G.Z. Cao, *Adv. Mater.* 19 (2007) 2588–2592.
- [13] K. Park, Q. Zhang, B.B. Garcia, X. Zhou, Y.-H. Jeong, G. Cao, *Adv. Mater.* 22 (2010) 2329–2332.
- [14] Q. Zhang, C.S. Dandeneau, X. Zhou, G. Cao, *Adv. Mater.* 21 (2009) 4087–4108.
- [15] Z.L. Wang, *Adv. Funct. Mater.* 18 (2008) 3553.
- [16] Z.L. Wang, *Adv. Mater.* 24 (2011) 280.
- [17] C. Xu, C. Pan, Y. Liu, Z.L. Wang, *Nano Energy* 1 (2012) 259–272.
- [18] X. Li, C. Gao, H. Duan, B. Lu, X. Pan, E. Xie, *Nano Energy* 1 (2012) 640–645.
- [19] Y.-Q. Bie, Z.-M. Liao, H.-Z. Zhang, G.-R. Li, Y. Ye, Y.-B. Zhou, J. Xu, Z.-X. Qin, L. Dai, D.-P. Yu, *Adv. Mater.* 23 (2011) 649.
- [20] Y. Yang, W. Guo, J. Qi, J. Zhao, Y. Zhang, *Appl. Phys. Lett.* 97 (2010) 223113.
- [21] D. Jezequel, J. Guenot, N. Jouini, F. Fievet, *Mater. Sci. Forum* 339 (1994) 152–153.
- [22] E.W. Seelig, B. Tang, A. Yamilov, H. Cao, R.P.H. Chang, *Mater. Chem. Phys.* 80 (2003) 257–263.
- [23] H.-M. Cheng, H.-C. Hsu, S.-L. Chen, W.-T. Wu, C.-C. Kao, L.-J. Lin, W.-F. Hsieh, *J. Crystal Growth* 277 (2005) 192–199.
- [24] Y.Y. Tay, S. Li, F. Boey, Y.H. Cheng, M.H. Liang, *Physica B: Condensed Matter* 394 (2007) 372–376.
- [25] T.-L. Phan, R. Vincent, D. Cherns, N.H. Dan, S.-C. Yu, *Appl. Phys. Lett.* 93 (2008) 082110–082113.
- [26] K. Keis, J. Lindgren, S.-E. Lindquist, A. Hagfeldt, *Langmuir* 16 (2000) 4688–4694.
- [27] D. Hwang, H. Lee, S.-Y. Jang, S.M. Jo, D. Kim, Y. Seo, D.Y. Kim, *ACS Appl. Mater. Interfaces* 3 (2011) 2719–2725.
- [28] Y.J. Kim, M.H. Lee, H.J. Kim, G. Lim, Y.S. Choi, N.-G. Park, K. Kim, W.I. Lee, *Adv. Mater.* 21 (2009) 3668–3673.
- [29] M. Itagaki, K. Hoshino, Y. Nakano, I. Shitanda, K. Watanabe, *J. Power Sources* 195 (2010) 6905–6923.
- [30] T. Zhai, L. Li, X. Wang, X. Fang, Y. Bando, D. Golberg, *Adv. Funct. Mater.* 20 (2010) 4233.
- [31] J. Zhou, Y. Gu, Y. Hu, W. Mai, P.-H. Yeh, G. Bao, A.K. Sood, D.L. Polla, Z.L. Wang, *Appl. Phys. Lett.* 94 (2009) 191103.
- [32] Y. Jin, J. Wang, B. Sun, J.C. Blakesley, N.C. Greenham, *Nano Lett.* 8 (2008) 1649.
- [33] J. Zou, Q. Zhang, K. Huang, N. Marzari, *J. Phys. Chem. C* 114 (2010) 10725.
- [34] X. Li, C. Gao, H. Duan, B. Lu, Y. Wang, L. Chen, Z. Zhang, X. Pan, E. Xie, *Small* (2013), <http://dx.doi.org/10.1002/sml.201202408>.
- [35] E. Monroy, F. Omnès, F. Calle, *Semicond. Sci. Technol.* 18 (2003) R33.
- [36] X. Li, C. Gao, J. Wang, B. Lu, W. Chen, J. Song, S. Zhang, Z. Zhang, X. Pan, E. Xie, *J. Power Sources* 214 (2012) 244–250.